J. Fluid Mech. (2023), *vol*. 970, A15, doi:10.1017/jfm.2023.590

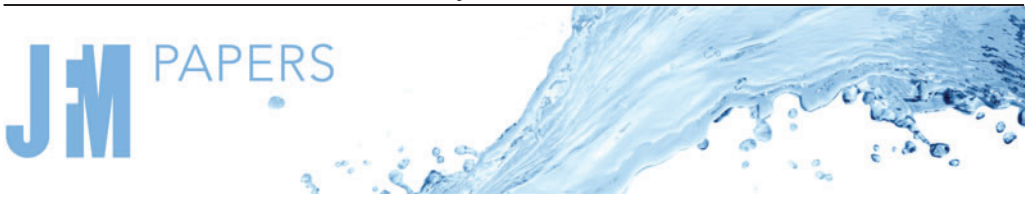

Asymmetric secondary flows above geometrically symmetric surface roughness

Wen Zhang[1,2], **Xiang I.A. Yang**[3,†], **Xiaowei Zhu**[4], **Minping Wan**[1,2,†] and **Shiyi Chen**[5,1,2]

[1]Guangdong Provincial Key Laboratory of Turbulence Research and Applications, Department of Mechanics and Aerospace Engineering, Southern University of Science and Technology, Shenzhen 518055, PR China

[2]Guangdong-Hong Kong-Macao Joint Laboratory for Data-Driven Fluid Mechanics and Engineering Applications, Southern University of Science and Technology, Shenzhen 518055, PR China

[3]Mechanical Engineering, Pennsylvania State University, PA 16802, USA

[4]Department of Mechanical Engineering, Portland State University, Portland, OR 97201, USA

[5]Eastern Institute for Advanced Study, Ningbo 315200, PR China

(Received 11 January 2023; revised 25 June 2023; accepted 9 July 2023)

The mean flow behaviour of a turbulent boundary layer over rough walls is expected to exhibit symmetries that govern the flow dynamics. In particular, when roughness elements are arranged in a spanwise symmetric manner, the mean flow above them should also exhibit spanwise symmetry. This symmetrical consideration has garnered substantial empirical support. We conduct direct numerical simulations (DNS) of flow over aligned cube arrays to test such symmetry considerations further. We vary the surface coverage density from 0.25 % to 6.25 %, and employ an averaging time of about 100 large-eddy turnover times, which is longer than the typical averaging time in prior DNS studies of rough-wall boundary layers. The results suggest the presence of spanwise asymmetry in the mean flow. Specifically, we observe the development of a prominent secondary vortex on one side of the cubical roughness, accompanied by a relatively smaller secondary vortex on the other side. This asymmetry becomes most pronounced when the surface coverage density is approximately 0.59 %, and diminishes as the coverage density approaches either a low or a high value. We also establish that this mean flow asymmetry is robust across variations in the domain size, the initial condition, and the placement of the cubes in the spanwise direction.

Key words: turbulent boundary layers, turbulence theory, turbulence simulation

† Email addresses for correspondence: xzy48@psu.edu, wanmp@sustech.edu.cn

1. Introduction

Turbulence is known to be stochastic, but its statistics are expected to reflect the symmetries that constrain it. An example is the flat-plate boundary layer, where the flow is statistically symmetric in the spanwise direction owing to the statistical homogeneity. Symmetry properties of turbulence like the one above have received considerable empirical support and are common in fluid flow modelling (Pope 2000). In recent developments of machine learning models, constraints such as symmetry or invariance properties are invoked to improve the training efficiency (Ling, Kurzawski & Templeton 2016; Duraisamy, Iaccarino & Xiao 2019; Brunton, Noack & Koumoutsakos 2020). Deviations from symmetry considerations are often attributed to a lack of statistical convergence or numerics. For instance, Grandemange, Gohlke & Cadot (2013, 2014) found asymmetry in a wake flow, but the asymmetry vanishes when the averaging time is sufficiently long. The goal of this work is to test such symmetry considerations in the context of flow over aligned cube arrays.

1.1. *Roughness-induced large-scale secondary flows*

The dominant dynamics within a flat-plate boundary layer are characterized by self-sustaining cycles in the inner layer (Jimenez & Moin 1991), as well as the presence of large-scale motions (Adrian 2007; Hutchins & Marusic 2007) and very-large-scale motions in the outer layer (Kim & Adrian 1999; Balakumar & Adrian 2007; Dennis & Nickels 2011*a*,*b*). However, the introduction of surface roughness disrupts the self-sustaining cycle, transforming the inner layer into the roughness sublayer. Within this sublayer, the flow is a combination of roughness wakes and a shear layer riding atop the roughness elements (Yang *et al.* 2016; Aghaei-Jouybari *et al.* 2022; Zhang *et al.* 2022). The roughness sublayer extends approximately 3–5 times the roughness height (Raupach, Antonia & Rajagopalan 1991; Flack, Schultz & Connelly 2007). Beyond the roughness sublayer, the flow characteristics resemble those of a flat-plate boundary layer (Jiménez 2004; Castro 2007; Schultz & Flack 2007; Leonardi & Castro 2010; Flack & Schultz 2014; Chung, Monty & Hutchins 2018; Chung *et al.* 2021).

In the past decade, significant attention has been devoted to studying roughness-induced secondary motions that extend beyond the roughness sublayer. Pioneering studies by Mejia-Alvarez & Christensen (2013) and Barros & Christensen (2014) were among the first to report these secondary motions. In their investigations, these large-scale secondary motions manifest as spanwise alternating high- and low-momentum pathways in the mean flow. Similar secondary motions have been observed above herringbone-like roughness (Nugroho, Hutchins & Monty 2013), spanwise alternating high- and low-roughness stripes (Willingham *et al.* 2014), and spanwise heterogeneous super-hydrophobic surfaces (Jelly, Jung & Zaki 2014; Lee, Jelly & Zaki 2015). Moreover, similar secondary motions arise in other contexts. In fact, secondary motions arise as long as the Reynolds stresses are spanwise heterogeneous (Anderson *et al.* 2015). The strength of these large-scale secondary motions is by and large determined by the length scale of the spanwise heterogeneity (Vanderwel & Ganapathisubramani 2015; Chan *et al.* 2018; Yang & Anderson 2018; Yang *et al.* 2019). The secondary motions are the strongest when the spanwise length scale is comparable to the boundary-layer height. Other factors also affect the strength of the secondary motions. The impacts of thermal stratification, roughness geometry and roughness arrangements have been investigated by Forooghi, Yang & Abkar (2020), Medjnoun, Vanderwel & Ganapathisubramani (2020) and Viggiano *et al.* (2022), respectively. Nonetheless, the aforementioned studies did not report statistically significant asymmetries in the mean flow, which is the focus of our current investigation.

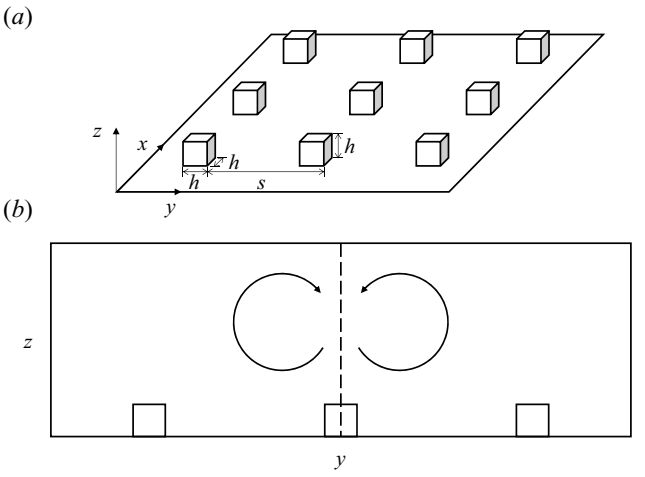

Figure 1. (*a*) A sketch of the cubical roughness, where x, y, z are the streamwise, spanwise and vertical directions, respectively, h is the roughness height, and s is the spacing between adjacent roughness elements. The roughness is arranged in an aligned configuration. (*b*) A sketch of the roughness-induced large-scale secondary vortices in the spanwise-vertical (y–z) plane. The vertical dashed line across the cube centre shows the symmetry plane.

1.2. *This work*

We consider flow above aligned cubes as shown in figure 1(*a*). Aligned cubes induce secondary flows of the second kind, which manifest as counter-rotating vortices, as depicted in figure 1(*b*). The direction of these secondary flows, whether they bring low- or high-momentum fluid to the cubes, depends on the surface coverage density (Vanderwel & Ganapathisubramani 2015; Xu *et al.* 2021). In figure 1, the secondary motions bring high-momentum fluid to the cubes. These secondary flows are part of the mean flow, and they are expected to exhibit the symmetry that constrains flow. Specifically, the secondary flows should possess spanwise symmetry, with the symmetry plane indicated by the vertical dashed line across the cube centre in figure 1(*b*). Empirical evidence strongly supports this anticipated symmetry (Coceal *et al.* 2006; Cheng *et al.* 2007; Cheng & Porté-Agel 2015; Yang 2016; Yang *et al.* 2016; Basley, Perret & Mathis 2019; Xu *et al.* 2021). In this paper, we aim to re-evaluate this expected symmetry using direct numerical simulations (DNS).

The remainder of the paper is organized as follows. In § 2, we provide a detailed description of the DNS set-up. We employ an averaging time that exceeds the typical duration used in prior DNS studies of rough-wall boundary-layer flows. The results are presented in § 3. In § 4, we demonstrate that the observed asymmetry persists across variations in numerical techniques, domain sizes, the arrangement of cubes in the spanwise direction, and Reynolds numbers. Finally, concluding remarks are provided in § 5.

2. Direct numerical simulations

Creating a perfectly symmetric laboratory facility can be a challenging, if not impossible, task. However, such limitations are non-existent in numerical simulations. In our study, we conduct DNS of a half-channel flow with cubical roughness on the bottom wall.

For our DNS, we utilize the pseudo-spectral code LESGO, which solves the incompressible Navier–Stokes equations. The code employs a pseudo-spectral method

Case	Re_τ	s/h	λ_p	$L_x/h \times L_y/h \times L_z/h$	$n_x \times n_y$	$\Delta x^+ (= \Delta y^+)$	Δz^+	Tu_τ/L_z	TU_0/L_z
S04	360	4	6.25 %	40 × 20 × 6	10 × 5	3.75	0.5–3	88	1002
S06	360	6	2.78 %	42 × 24 × 6	7 × 4	3.75	0.5–3	77	1002
S08	360	8	1.56 %	40 × 24 × 6	5 × 3	3.75	0.5–3	122	1670
S10	360	10	1.00 %	40 × 20 × 6	4 × 2	3.75	0.5–3	115	1670
S13	360	13	0.59 %	39 × 26 × 6	3 × 2	3.75	0.5–3	110	1670
S15	360	15	0.44 %	45 × 30 × 6	3 × 2	3.75	0.5–3	101	1670
S20	360	20	0.25 %	40 × 40 × 6	2 × 2	3.75	0.5–3	93	1670
S13R	360	13	0.59 %	39 × 26 × 6	3 × 2	3.75	0.5–3	109	1670
S13X1	360	13	0.59 %	78 × 52 × 6	6 × 4	3.75	0.5–3	102	1670
S13X2	360	13	0.59 %	156 × 26 × 6	12 × 2	3.75	0.5–3	99	1670
S10X1	360	10	1.00 %	40 × 40 × 6	4 × 4	3.75	0.5–3	113	1670
S10X2	360	10	1.00 %	40 × 40 × 6	4 × 4	3.75	0.5–3	113	1670
L06	180	6	2.78 %	42 × 24 × 6	7 × 4	3.75	0.25–1.5	105	1163
L08	180	8	1.56 %	40 × 24 × 6	5 × 3	3.75	0.25–1.5	93	1163
L10	180	10	1.00 %	40 × 20 × 6	4 × 2	3.75	0.25–1.5	89	1163
L15	180	15	0.44 %	45 × 30 × 6	3 × 2	3.75	0.25–1.5	77	1163
L20	180	20	0.25 %	40 × 40 × 6	2 × 2	3.75	0.25–1.5	73	1163

Table 1. DNS details. The domain is a half-channel; $Re_\tau = L_z u_\tau/\nu$ is the friction Reynolds number, where u_τ is the friction velocity; s and h are the spacing and height of cubical roughness elements, respectively; λ_p is the surface roughness coverage density; L_x, L_y and L_z are the sizes of the domain in the streamwise, spanwise and wall-normal directions, respectively; $n_x \times n_y$ are the sizes of the cube array; and Δx^+, Δy^+ and Δz^+ are the grid spacings in the three directions normalized by viscous scales. The grid is uniform in horizontal directions and stretched in the vertical direction; T is statistical time; and U_0 is the mean streamwise velocity at the top of the domain. S10X1, S10X2 differ in their roughness arrangements.

in the streamwise and spanwise directions, while using a second-order finite difference method in the wall-normal direction. The domain is periodic in the streamwise and spanwise directions, with a stress-free top boundary. To resolve the roughness, we employ an immersed boundary method (Chester, Meneveau & Parlange 2007). The code has been extensively validated and used for simulating boundary-layer flows, including those over complex terrains (Anderson *et al.* 2015; Yang & Meneveau 2016, 2017), vegetative canopies (Chester *et al.* 2007; Bai, Meneveau & Katz 2012) and urban canopies (Cheng & Porté-Agel 2015; Giometto *et al.* 2016; Yang *et al.* 2019; Zhang *et al.* 2022). Further details of the code are omitted here for the sake of brevity.

Table 1 provides an overview of our DNS set-up. We consider aligned cube arrays as the surface roughness, with a surface coverage density or solidity ranging from 0.25 % to 6.25 %. The domain height $L_z = 6h$ is fixed, while the streamwise and spanwise dimensions of the domains satisfy $L_x \geq 2\pi L_z$ and $L_y \geq \pi L_z$ (Lozano-Durán & Jiménez 2014). The grid is uniform in the horizontal directions, with fixed grid spacing $\Delta x^+ = \Delta y^+ = 3.75$. In the vertical direction, the grid is stretched to achieve resolution $\Delta z^+_{min} \approx 0.5$ near the wall and $\Delta z^+_{max} \approx 3$ at the top of the domain. This grid resolution is comparable to, and often finer than, that used in previous works (Coceal *et al.* 2006; Leonardi & Castro 2010; MacDonald *et al.* 2018). In all DNS, the surfaces of the cubes coincide with the surfaces of the computational cells to give an accurate representation of the cube geometry.

Our baseline cases are denoted as S[s/h], where s represents the spacing between neighbouring cubes, and h denotes the cube height. We vary s from $4h$ to $20h$, resulting

Averaging time	Reference
$T = 100\delta/u_\tau$	Coceal *et al.* (2006)
$T = 50\delta/u_\tau$	Yuan & Piomelli (2014)
$T \approx 25\delta/u_\tau$	Chan *et al.* (2015)
$T \approx 10\delta/u_\tau$	Mazzuoli & Uhlmann (2017)
$T \approx 30\delta/u_\tau$	Ismail *et al.* (2018)
$T \approx 50\delta/u_\tau$	Chung *et al.* (2018)
$T \approx 14\delta/u_\tau$	Wu *et al.* (2019)
$T = 50\delta/u_\tau$	Ma *et al.* (2021)
$T = 1.5\delta/u_\tau$	Ganju *et al.* (2022)

Table 2. Averaging time used in prior DNS studies of rough-wall boundary-layer flows. Here, δ/u_τ is large-eddy turnover time, where δ is half-channel height/boundary layer thickness/pipe radius. This is not meant to be a comprehensive list.

in cases S04, S06, S08, S10, S13, S15 and S20. Additionally, we explore variations in the initial condition and domain size. This leads to S13R, which involves flipping the spanwise coordinate of S13 to verify that any observed mean flow asymmetry is not an artefact of the numerics, and S13X1 and S13X2, where we double and quadruple the streamwise size of the S13 domain, respectively, to confirm the robustness of the observed asymmetry to changes in domain dimensions. To study the effects of the spanwise size of the domain, we add cases S10X1, S10X2 and S13X1, where we double the spanwise size of the S10 and S13 domains. Finally, we investigate the effect of cube placement in the spanwise direction, resulting in cases S10X1 and S10X2, where the roughness in S10X2 is shifted spanwise relative to S10X1. The purpose of these cases is to demonstrate that the location of the cubes does not influence the observed asymmetry.

The S[s] cases are conducted at a friction Reynolds number $Re_\tau = 360$, where $u_\tau = \sqrt{(1/\rho)L_z\,\mathrm{d}P/\mathrm{d}x}$ represents the friction velocity, L_z is the height of the half-channel, $\mathrm{d}P/\mathrm{d}x$ is the pressure gradient driving the flow, and ρ is the fluid density. To examine whether the observed asymmetry is unique to a specific Reynolds number, we perform additional five DNS at $Re_\tau = 180$, denoted as L06, L08, L10, L15 and L20. These lower Reynolds number simulations are chosen as the flow is already in the fully rough regime at $Re_\tau = 360$, and increasing the Reynolds number is unlikely to significantly alter the flow phenomena. We use an averaging time ranging between 80 and 120 large-eddy turnover times, where L_z/u_τ corresponds to one large-eddy turnover time. Table 2 provides a summary of the averaging times used in some of the prior DNS studies of rough-wall boundary layers. The typical averaging time is 10–50 large-eddy turnover times, except that $100L_z/u_\tau$ is used by Coceal *et al.* (2006), which is comparable to our averaging time. Our chosen averaging time is longer than the typical averaging time and is twice as long as what Yuan & Piomelli (2014) considered sufficient for obtaining converged mean flow statistics.

3. Results

We present the results of the baseline cases in this section. Figure 2 shows the contours of the streamwise and temporally averaged velocities $\langle\bar{u}\rangle_x$ in the spanwise–vertical (y–z) plane. The in-plane motions are shown via $(\langle\bar{v}\rangle_x, \langle\bar{w}\rangle_x)$ vectors. Here, u, v, w are the velocities in the streamwise (x), spanwise (y) and vertical (z) directions, respectively, the overbar denotes time averaging, $\langle\cdot\rangle$ denotes spatial average, and the subscript is the direction of averaging. The symmetry plane is located at the cube centre ($y = 0$).

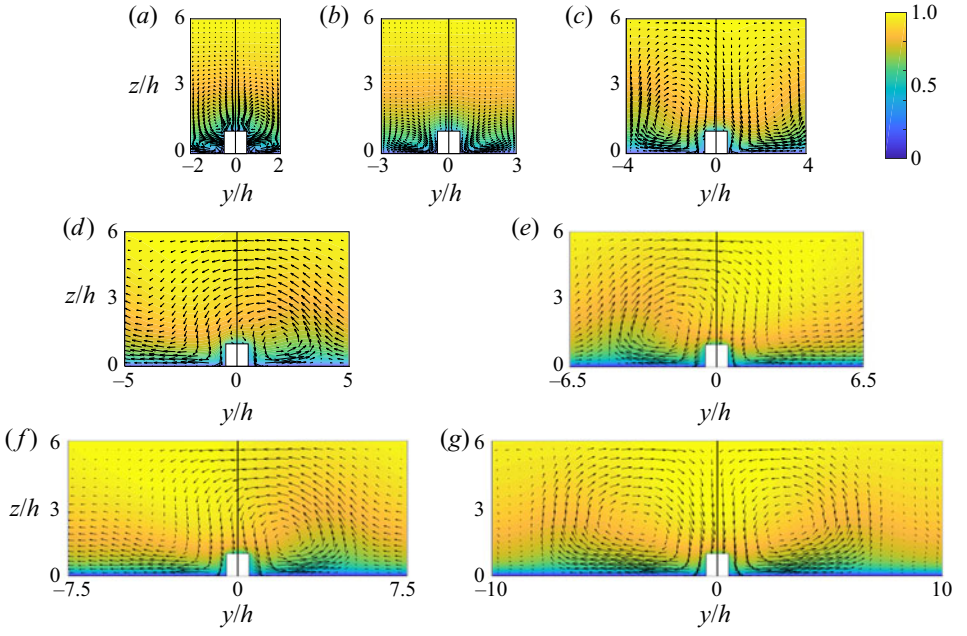

Figure 2. Contours of the streamwise and temporally averaged streamwise velocity $\langle\bar{u}\rangle_x$ in the spanwise/wall-normal plane. The velocity is normalized by its average at the top boundary, which we denote as U_0. The vectors indicate the in-plane motions, i.e. $(\langle\bar{v}\rangle_x, \langle\bar{w}\rangle_x)$. The origin of the spanwise coordinate is placed at the centre of the roughness element. The roughness is symmetric with respect to $y = 0$. The spanwise extent of the plot equals the distance between two neighbouring roughness elements, which is the minimum repeating unit of the flow. Cases are (*a*) S04, (*b*) S06, (*c*) S08, (*d*) S10, (*e*) S13, (*f*) S15, and (*g*) S20.

Large-scale secondary motions that span the entire boundary layer are found when $s/h > 6$. In S04, S06 and S20, the secondary motions are approximately symmetric with respect to $y = 0$, which aligns with previous findings. Previous authors have also reported spanwise symmetric mean flow above aligned cubes with surface coverage density $\gtrsim 3\,\%$ (Yang *et al.* 2016; Xu *et al.* 2021), which corresponds to S04 and S06 in our study. Additionally, the flow above isolated cubes, a good approximation for case S20, is known to exhibit spanwise symmetry (Wang & Lam 2019).

However, what is unexpected is the spanwise asymmetry in the mean flows in cases S08, S10, S13 and S15. In these cases, we observe a significant vortex on one side of the roughness, while no such large vortex is present on the other side. These secondary vortices enhance the vertical transport of streamwise momentum, resulting in the spanwise undulation of $\langle\bar{u}\rangle_x$ as revealed by the contour plots.

To obtain a more quantitative measure of the mean flow asymmetry, we examine the velocities on the symmetry plane at $y = 0$. Figure 3 displays the streamwise and temporally averaged velocities at the cube centre (cc), denoted as $\langle\bar{u}\rangle_{x,cc}$, $\langle\bar{v}\rangle_{x,cc}$ and $\langle\bar{w}\rangle_{x,cc}$. In a symmetric flow with respect to $y = 0$, the spanwise velocity $\langle\bar{v}\rangle_{x,cc}$ would be zero at $y = 0$. As seen in S04 and S06, where the flow exhibits spanwise symmetry, $\langle\bar{v}\rangle_{x,cc}$ is indeed close to zero at $y = 0$. However, in cases S10, S13 and S15, there is a noticeable deviation of $\langle\bar{v}\rangle_{x,cc}$ from zero, indicating the presence of mean flow asymmetry. While not as prominent as in cases S10 or S15, a non-zero value of $\langle\bar{v}\rangle_{x,cc}$ is also observed in S20, indicating a weak mean flow asymmetry in this case. The behaviours of $\langle\bar{u}\rangle_{x,cc}$ and $\langle\bar{w}\rangle_{x,cc}$ align with findings reported in the literature. Specifically, $\langle\bar{u}\rangle_{x,cc}$ increases with increasing inter-cube

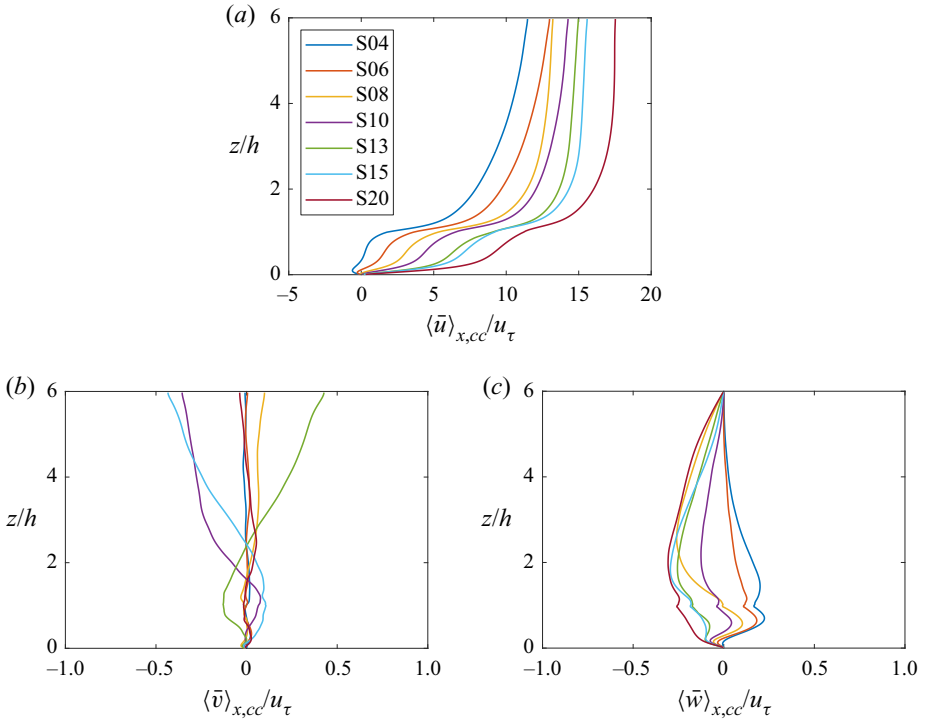

Figure 3. Streamwise and temporally averaged velocities at the cube centreline (i.e. $y = 0$ in figure 2): (*a*) $\langle\bar{u}\rangle_{x,cc}/u_\tau$, (*b*) $\langle\bar{v}\rangle_{x,cc}/u_\tau$, and (*c*) $\langle\bar{w}\rangle_{x,cc}/u_\tau$.

distance due to the decreasing drag force in the k-type roughness regime. This trend is consistent with previous studies. In terms of $\langle\bar{w}\rangle_{x,cc}$, a downwelling motion leads to a negative value in cases S08, S10, S13, S15 and S20, similar to the observations made by Willingham *et al.* (2014), Anderson *et al.* (2015) and Chung *et al.* (2018). On the other hand, an upwelling motion results in a positive $\langle\bar{w}\rangle_{x,cc}$ in S04, which is in line with the findings of Xu *et al.* (2021).

Figures 4(*a–g*) show the streamwise, wall-normal and time-averaged x velocity $\langle\bar{u}\rangle_{x,z}/U_b$ as a function of the spanwise coordinate, which is also a good measure of the mean flow asymmetry. Here, $U_b = \langle\bar{u}\rangle_{x,y,z}$ is the mean flow rate. We see that the flow is roughly spanwise symmetric in S04, S06 and S20, and spanwise asymmetric in S08, S10, S13 and S15. The dip at $y = 0$ is due to the roughness that blocks the flow. The other dips in the S08, S10, S15 and S20 results are due to secondary motions, which bring low-speed fluid in the wake of the cube to its sides.

Finally, we define

$$\Delta U(y) \equiv \left|\langle\bar{u}\rangle_{x,z}(y) - \langle\bar{u}\rangle_{x,z}(-y)\right|, \tag{3.1}$$

and $\max_y[\Delta U]$ and $\langle[\Delta U]\rangle_y$, i.e. the maximum of ΔU and the average of ΔU, are one-number measures of the mean flow asymmetry, with $\Delta U(y) = 0$ if the flow is spanwise symmetric. Figure 5 shows $\langle\Delta U\rangle_y$ and $\max_y[\Delta U]$ as functions of the inter-cube distance s. Both measures are approximately 0 in S04 and S06. They increase as s/h increases, and peak when $s/h = 15$. The peak values are 0.07 and 0.12 for $\langle[\Delta U]\rangle_y/U_b$

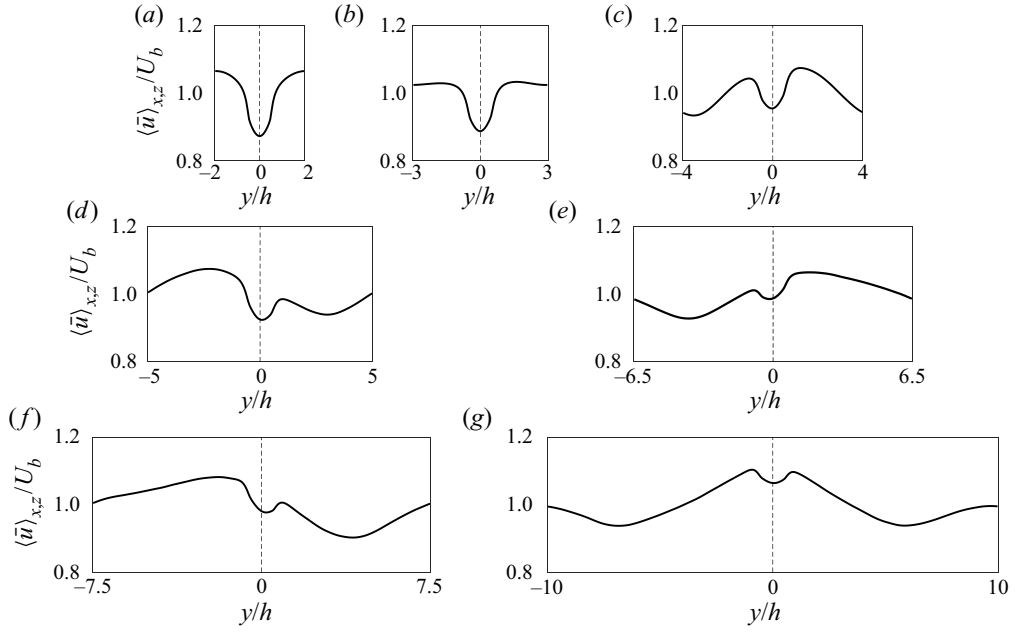

Figure 4. Streamwise and normal averaged mean velocity $\langle\bar{u}\rangle_{x,z}$ as a function of the spanwise coordinate for (*a*) S04, (*b*) S06, (*c*) S08, (*d*) S10, (*e*) S13, (*f*) S15, and (*g*) S20. We show results in one repeating unit for brevity. The origin of the spanwise coordinate is at the centre of the roughness element.

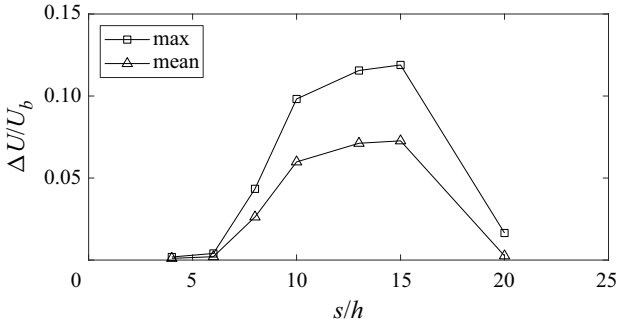

Figure 5. The maximum (square symbols) and the mean (triangle symbols) of $\Delta U/U_b$ as a function of the inter-cube distance.

and $\max_y[\Delta U]/U_b$, respectively, suggesting that the asymmetry can be as large as 10 % of the bulk velocity.

4. Discussion

4.1. *Numerics, domain size and Reynolds number*

In this subsection, we show that the mean flow asymmetry is robust to variations in the domain size, the direction of the spanwise axis, the spanwise location of the surface roughness, the initial condition, and the Reynolds number.

In our case, the averaging time exceeds 100 large-eddy turnover times. We examine the momentum budget and the premultiplied velocity probability density function (p.d.f.).

Consider a generic flow quantity ϕ. Time averaging is sufficient if $\partial\bar{\phi}/\partial t = 0$, i.e. if the other terms in the ϕ transport equation balance. The transport equation of the streamwise velocity reads

$$\frac{\mathrm{d}\langle\bar{u}\rangle_{x,y}}{\mathrm{d}t} = -\left\langle\frac{1}{\rho}\frac{\partial\bar{p}}{\partial x}\right\rangle_{x,y} - \frac{\mathrm{d}\langle\overline{u'w'}\rangle_{x,y}}{\mathrm{d}z} - \frac{\mathrm{d}\langle\overline{u''w''}\rangle_{x,y}}{\mathrm{d}z} + \nu\frac{\mathrm{d}^2\langle\bar{u}\rangle_{x,y}}{\mathrm{d}z^2} \tag{4.1}$$

outside the roughness occupied layer, where $u'' = u - \langle\bar{u}\rangle_{x,y}$ and $w'' = w - \langle\bar{w}\rangle_{x,y}$. The terms on the right-hand side are the mean pressure gradient term, the turbulent stress term, the dispersive stress term and the viscous stress term. If time averaging is sufficient, then the terms on the right-hand side should balance, leading to

$$-\langle\overline{u'w'}\rangle^+_{x,y} - \langle\overline{u''w''}\rangle^+_{x,y} + \frac{1}{Re_\tau}\frac{\mathrm{d}\langle\bar{u}\rangle^+_{x,y}}{\mathrm{d}z^+} = 1 - \frac{z}{L_z}, \tag{4.2}$$

which indicates that the sum of Reynolds stress, dispersive stress and viscous stress is a linear function of the wall-normal coordinate z. This balance is confirmed by the results shown in figure 6. In addition to the momentum budget, we evaluate the averaging time through the premultiplied velocity p.d.f. (Meneveau & Marusic 2013; de Silva *et al.* 2017). Figure 7 shows the premultiplied p.d.f. of u', v', w' in case S13 at two locations, i.e. $z/h = 5$ and $z/h = 3$, above the cube centre. We see that the mean flow, which is the area under the curve, is captured accurately. The results are similar at other locations and in other cases, and are not shown here for brevity. Nonetheless, further investigation may still be needed to confirm the statistical convergence.

Next, we explore the effects of inverting the spanwise axis to examine the sustainability of the observed asymmetry. According to the spanwise symmetry of the Navier–Stokes equations, if the asymmetry is inherent to the flow, then flipping the y axis and the spanwise velocity components should result in sustained asymmetry. We define the flipped quantities as

$$u_{flip}(x, y, z) = u(x, -y, z), \quad v_{flip}(x, y, z) = -v(x, -y, z), \quad w_{flip}(x, y, z) = w(x, -y, z). \tag{4.3a–c}$$

If numerics are responsible for the asymmetry, then $\boldsymbol{u}_{flip}$ would not be able to sustain itself and would revert back to $\boldsymbol{u}$. Flipping the y axis and the spanwise velocity in case S13 leads to case S13R. Figure 8 shows the contours of $\langle\bar{u}\rangle_x$ in S13R. The mean asymmetry sustains for more than another 100 large-eddy turnover times. Consequently, we conclude that numerics are not responsible for the observed asymmetries.

Third, we investigate the effect of domain size. The size of our domain is comparable to those in the literature (Lozano-Durán & Jiménez 2014; Yang *et al.* 2019; Xu *et al.* 2021) and should be sufficient. To further verify the adequacy of our domain size, we conduct two additional DNS: S13X1 with a domain twice as long and twice as wide as that of S13, and S13X2 with a domain four times as long as that of S13. Figures 9(*a*,*b*) show the contours of the mean flow, and the same asymmetry is observed. Hence we conclude that the finite domain size is not a concern.

Fourth, we investigate the effect of the spanwise location of the cubes. Figure 10 shows the contours of the mean velocity in S10X1 and S10X2, where the cubes in S10X2 are displaced in the spanwise direction by $0.25s$ relative to S10X1. We see that the mean flow asymmetry persists, suggesting that spanwise location of the cubes should not affect the mean flow asymmetry. The result here also shows that the implementation of the periodic boundary condition in the spanwise direction does not affect the mean flow asymmetry.

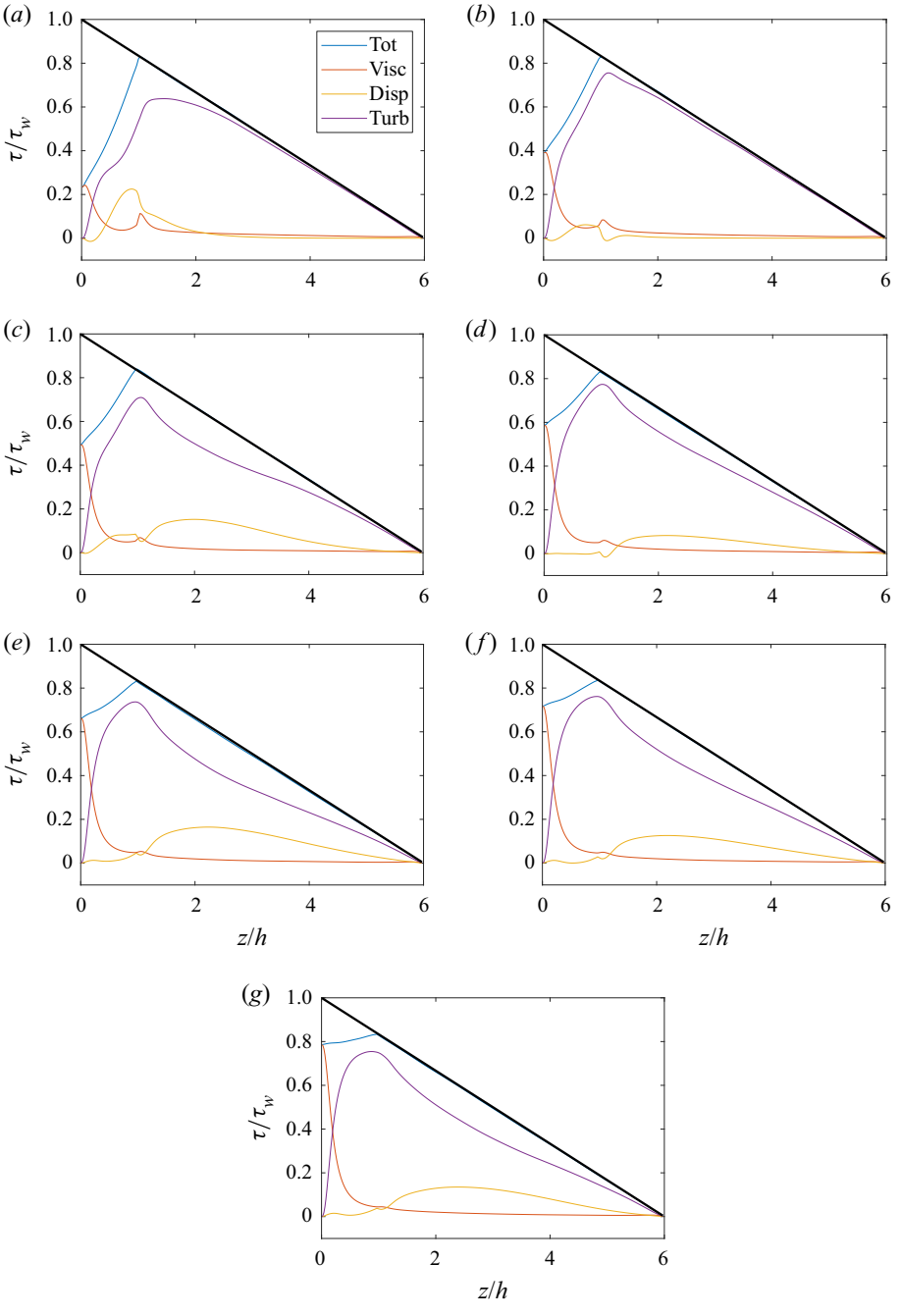

Figure 6. Terms in (4.2), i.e. the momentum budget equation, for (*a*) S04, (*b*) S06, (*c*) S08, (*d*) S10, (*e*) S13, (*f*) S15, and (*g*) S20. Here, Tot, Vis, Disp and Turb are short for total stress, viscous stress, dispersive stress and turbulent stress.

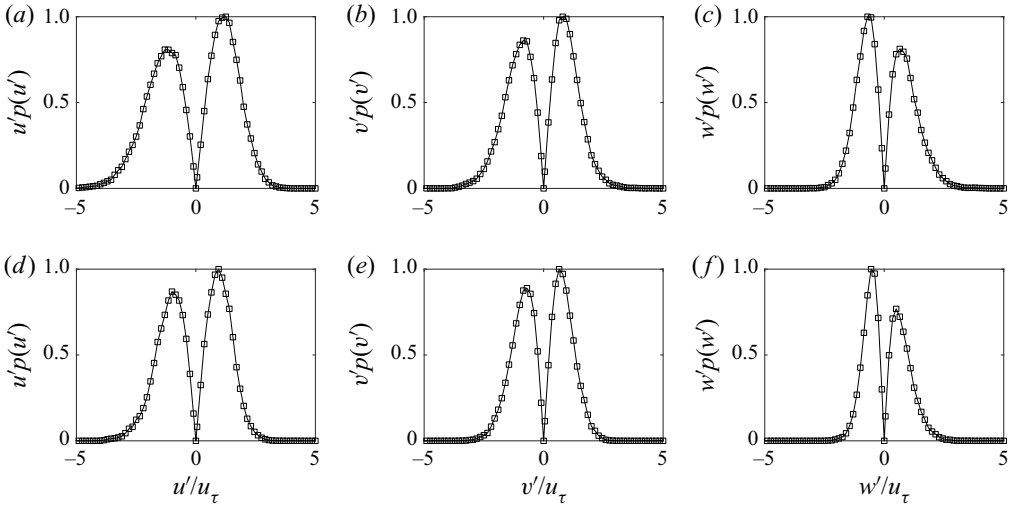

Figure 7. Premultiplied probability density functions of velocity fluctuations $u'\,p(u')$, $v'\,p(v')$, $w'\,p(w')$ at (*a–c*) $z/h = 3$ and (*d–f*) $z/h = 5$ above the cube centre in case S13. The premultiplied probability density function has been normalized such that the maximum is 1.

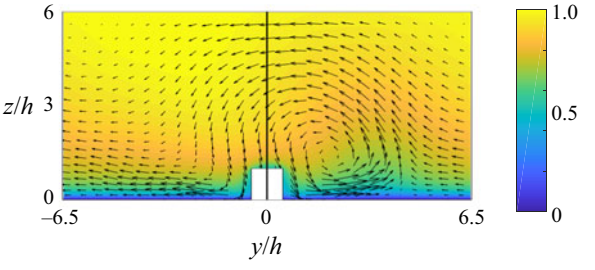

Figure 8. Same as figure 2, but for S13R.

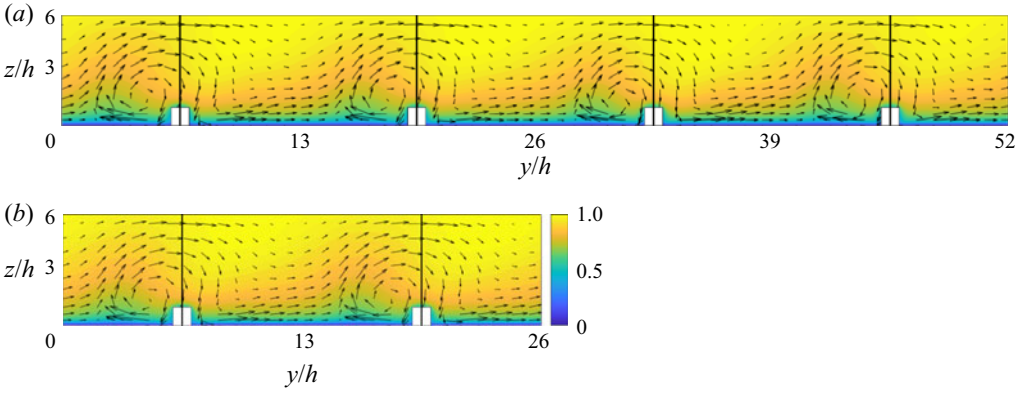

Figure 9. Same as figure 2, but for (*a*) S13X1, (*b*) S13X2. Here, we show the full extent of the domain in the spanwise direction.

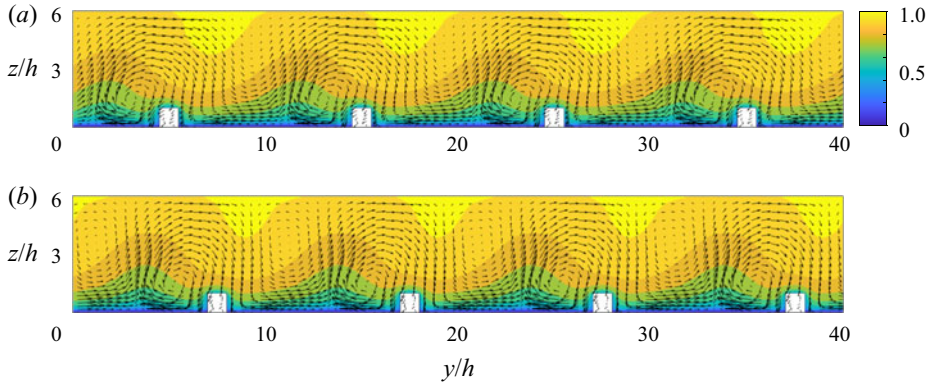

Figure 10. Same as figure 2, but for (*a*) S10X1, (*b*) S10X2. Here, we show the full extent of the domain in the spanwise direction.

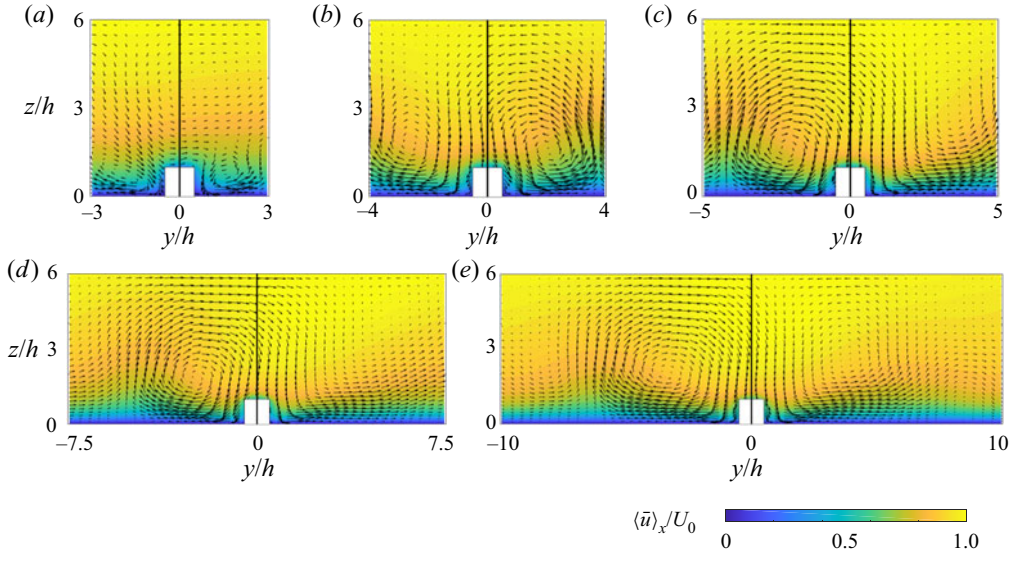

Figure 11. Same as figure 2, but for the $Re_\tau = 180$ cases: (*a*) L06, (*b*) L08, (*c*) L10, (*d*) L15, and (*e*) L20.

Finally, we investigate the effect of the Reynolds number. Figure 11 shows the results at $Re_\tau = 180$. We see that mean flow asymmetry exists at this low Reynolds number.

4.2. *A heuristic explanation*

Here, we attempt to explain the spanwise asymmetry in the mean flow. We know that the sizes of the secondary motions are constrained by both the height of the channel and the distance s between two neighbouring cubes (Vanderwel & Ganapathisubramani 2015). When s is sufficiently large, the sizes of the secondary motions are limited by the channel half-height, and its size is $O(L_z)$ – this is what we see in S20. In that case, a repeating unit that spans a distance s in the spanwise direction fits two secondary vortices, and the flow is spanwise symmetric. We call these secondary vortices developed vortices. When s is sufficiently small, the sizes of the secondary motions are limited by s – this is what

we see in S06. A repeating tile that spans a distance s in the spanwise direction also fits two of these secondary vortices, and again, the flow would be spanwise symmetric. We call these secondary vortices undeveloped vortices. When s is such that it does not fit two developed vortices but is too large for two undeveloped vortices, a repeating tile would fit one developed vortex and one undeveloped vortex, thereby giving rise to the asymmetry that we see in the previous subsection.

4.3. *Implication on the instantaneous flow field*

The discussion so far has focused on the secondary flows, which are mean flow features. In this subsection, we discuss the implication of the mean flow asymmetry on the instantaneous flow structures, which are large-scale motions, very-large-scale motions, and super-structures in a boundary layer. These structures extend in the streamwise direction from a few boundary-layer heights to a few hundred boundary-layer heights (Kim & Adrian 1999; Guala, Hommema & Adrian 2006; Balakumar & Adrian 2007; Hutchins & Marusic 2007; Monty *et al.* 2007; Kevin, Monty & Hutchins 2019). They are the most energetic motions in a boundary layer and are responsible for a lot of physical processes in a boundary layer (Smits, McKeon & Marusic 2011; Marusic & Monty 2019). The asymmetry found in this work provides a potential strategy to control these structures: one can place the roughness such that these motions appear less frequently in one region and more frequently in another.

Figure 12 is a visualization of the instantaneous flow field at $z/h = 2$ in case S13 at eight time instances that are equally spaced over an extended period of time. We highlight the high-speed streaks following the methodology in Kevin *et al.* (2019). We see that the high-speed streaks are more likely to appear on one side of the roughness elements than the other. Figure 13 shows the probability density function for observing a high-speed streak at a given y location. We see that we can skew the probability density function significantly in S08, S10, S13 and S15, making the high-speed steaks appear on one side more frequently than on the other side.

5. Concluding remarks

We conduct DNS of flow over aligned cube arrays with surface coverage densities from 0.25 % to 6.25 %. Our observations reveal the presence of mean flow asymmetry above spanwise symmetric cubical roughness when the spanwise distance between neighbouring roughness elements falls within the range 6–20, corresponding to a coverage density between 2.78 % and 0.25 %.

In-depth investigations demonstrate the robustness of this mean flow asymmetry across various factors, including domain size, initial conditions and grid collocation. Furthermore, the asymmetry persists at Reynolds numbers $Re_\tau = 360$ and 180, even after averaging for approximately 100 large-eddy turnover times. This discovery represents an intriguing flow phenomenon akin to those found in previous studies, such as Van Der Veen *et al.* (2016), Iyer *et al.* (2017) and Xia *et al.* (2018). Additionally, it presents a potential strategy for controlling streaks in boundary-layer flows.

However, the exact physical mechanism that is responsible for the observed asymmetry is not clear and is left for future investigation. We are also yet to confirm the presence of such asymmetry at significantly higher Reynolds numbers. Finally, the effects of rough-wall topology such as the streamwise distance between adjacent cubes, are also interesting topics for future research.

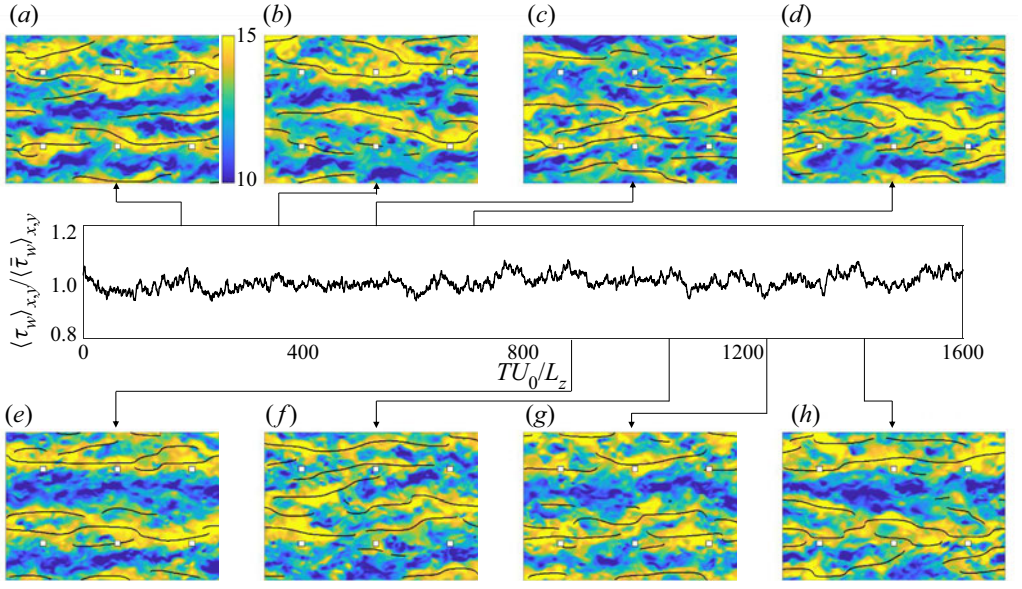

Figure 12. Contours of the instantaneous velocity u/u_τ at $z/h = 2$ in S13, and between them, the time history of the horizontally averaged instantaneous wall shear stress $\langle \tau_w \rangle_{x,y} / \langle \overline{\tau_w} \rangle_{x,y}$. The centrelines of the high-speed streaks are marked with the black lines in the contours. The squares show the locations of the cubes.

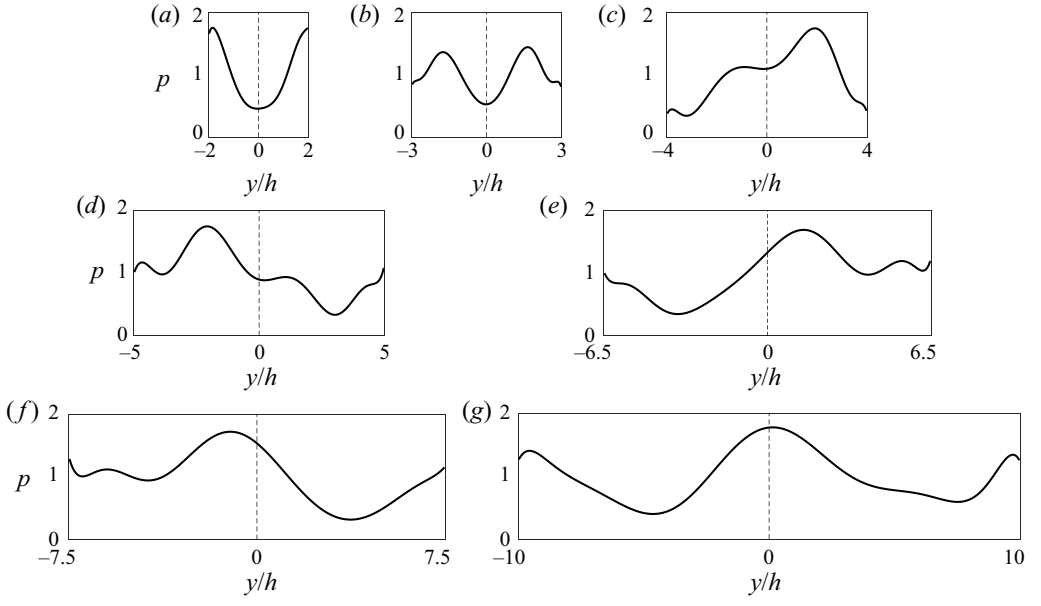

Figure 13. The occurrence probability of encountering a high-speed streak at a y location: (*a*) S04, (*b*) S06, (*c*) S08, (*d*) S10, (*e*) S13, (*f*) S15, and (*g*) S20. The probability has been normalized.

Funding. W.Z. and M.W. acknowledge NSFC (grant nos 12102168, and 11988102), Shenzhen Science & Technology Program (grant no. KQTD20180411143441009), Department of Science and Technology of Guangdong Province (grant nos 2019B21203001, 2020B1212030001), for financial support. X.I.A.Y. acknowledges NSF grant no. 500000021104 and Penn State University for financial support. Numerical

simulations have been supported by the Center for Computational Science and Engineering of Southern University of Science and Technology.

Declaration of interests. The authors report no conflict of interest.

Author ORCIDs.
Xiang I.A. Yang https://orcid.org/0000-0003-4940-5976;
Xiaowei Zhu https://orcid.org/0000-0003-1507-5681;
Minping Wan https://orcid.org/0000-0001-5891-9579.

References

Adrian, R.J. 2007 Hairpin vortex organization in wall turbulence. *Phys. Fluids* **19**, 041301.

Aghaei-Jouybari, M., Seo, J.-H., Yuan, J., Mittal, R. & Meneveau, C. 2022 Contributions to pressure drag in rough-wall turbulent flows: insights from force partitioning. *Phys. Rev. Fluids* **7** (8), 084602.

Anderson, W., Barros, J.M., Christensen, K.T. & Awasthi, A. 2015 Numerical and experimental study of mechanisms responsible for turbulent secondary flows in boundary layer flows over spanwise heterogeneous roughness. *J. Fluid Mech.* **768**, 316–347.

Bai, K., Meneveau, C. & Katz, J. 2012 Near-wake turbulent flow structure and mixing length downstream of a fractal tree. *Boundary-Layer Meteorol.* **143**, 285–308.

Balakumar, B.J. & Adrian, R.J. 2007 Large- and very-large-scale motions in channel and boundary-layer flows. *Phil. Trans. R. Soc. Lond.* A **365**, 665–681.

Barros, J.M. & Christensen, K.T. 2014 Observations of turbulent secondary flows in a rough-wall boundary layer. *J. Fluid Mech.* **748**, R1.

Basley, J., Perret, L. & Mathis, R. 2019 Structure of high Reynolds number boundary layers over cube canopies. *J. Fluid Mech.* **870**, 460–491.

Brunton, S.L., Noack, B.R. & Koumoutsakos, P. 2020 Machine learning for fluid mechanics. *Annu. Rev. Fluid Mech.* **52** (1), 477–508.

Castro, I.P. 2007 Rough-wall boundary layers: mean flow universality. *J. Fluid Mech.* **585**, 469–485.

Chan, L., MacDonald, M., Chung, D., Hutchins, N. & Ooi, A. 2015 A systematic investigation of roughness height and wavelength in turbulent pipe flow in the transitionally rough regime. *J. Fluid Mech.* **771**, 743–777.

Chan, L., MacDonald, M., Chung, D., Hutchins, N. & Ooi, A. 2018 Secondary motion in turbulent pipe flow with three-dimensional roughness. *J. Fluid Mech.* **854**, 5–33.

Cheng, H., Hayden, P., Robins, A. & Castro, I. 2007 Flow over cube arrays of different packing densities. *J. Wind Engng Ind. Aerodyn.* **95** (8), 715–740.

Cheng, W.-C. & Porté-Agel, F. 2015 Adjustment of turbulent boundary-layer flow to idealized urban surfaces: a large-eddy simulation study. *Boundary-Layer Meteorol.* **155** (2), 249–270.

Chester, S., Meneveau, C. & Parlange, M.B. 2007 Modeling turbulent flow over fractal trees with renormalized numerical simulation. *J. Comput. Phys.* **225**, 427–448.

Chung, D., Hutchins, N., Schultz, M.P. & Flack, K.A. 2021 Predicting the drag of rough surfaces. *Annu. Rev. Fluid Mech.* **53**, 439–471.

Chung, D., Monty, J.P. & Hutchins, N. 2018 Similarity and structure of wall turbulence with lateral wall shear stress variations. *J. Fluid Mech.* **847**, 591–613.

Coceal, O., Thomas, T., Castro, I. & Belcher, S. 2006 Mean flow and turbulence statistics over groups of urban-like cubical obstacles. *Boundary-Layer Meteorol.* **121**, 491–519.

Dennis, D.J. & Nickels, T.B. 2011*a* Experimental measurement of large-scale three-dimensional structures in a turbulent boundary layer. Part 1. Vortex packets. *J. Fluid Mech.* **673**, 180–217.

Dennis, D.J. & Nickels, T.B. 2011*b* Experimental measurement of large-scale three-dimensional structures in a turbulent boundary layer. Part 2. Long structures. *J. Fluid Mech.* **673**, 218–244.

Duraisamy, K., Iaccarino, G. & Xiao, H. 2019 Turbulence modeling in the age of data. *Annu. Rev. Fluid Mech.* **51** (1), 357–377.

Flack, K.A. & Schultz, M.P. 2014 Roughness effects on wall-bounded turbulent flows. *Phys. Fluids* **26**, 101305.

Flack, K.A., Schultz, M.P. & Connelly, J.S. 2007 Examination of a critical roughness height for outer layer similarity. *Phys. Fluids* **19**, 095104.

Forooghi, P., Yang, X.I.A. & Abkar, M. 2020 Roughness-induced secondary flows in stably stratified turbulent boundary layers. *Phys. Fluids* **32**, 105118.

GANJU, S., BAILEY, S. & BREHM, C. 2022 Amplitude and wavelength scaling of sinusoidal roughness effects in turbulent channel flow at fixed $Re_\tau = 720$. *J. Fluid Mech.* **937**, A22.

GIOMETTO, M.G., CHRISTEN, A., MENEVEAU, C., FANG, J., KRAFCZYK, M. & PARLANGE, M.B. 2016 Spatial characteristics of roughness sublayer mean flow and turbulence over a realistic urban surface. *Boundary-Layer Meteorol.* **160** (3), 425–452.

GRANDEMANGE, M., GOHLKE, M. & CADOT, O. 2013 Turbulent wake past a three-dimensional blunt body. Part 1. Global modes and bi-stability. *J. Fluid Mech.* **722**, 51–84.

GRANDEMANGE, M., GOHLKE, M. & CADOT, O. 2014 Turbulent wake past a three-dimensional blunt body. Part 2. Experimental sensitivity analysis. *J. Fluid Mech.* **752**, 439–461.

GUALA, M., HOMMEMA, S.E. & ADRIAN, R.J. 2006 Large-scale and very-large-scale motions in turbulent pipe flow. *J. Fluid Mech.* **554**, 521–542.

HUTCHINS, N. & MARUSIC, I. 2007 Evidence of very long meandering features in the logarithmic region of turbulent boundary layers. *J. Fluid Mech.* **579**, 1–28.

ISMAIL, U., ZAKI, T. & DURBIN, P. 2018 Simulations of rib-roughened rough-to-smooth turbulent channel flows. *J. Fluid Mech.* **843**, 419–449.

IYER, K.P., BONACCORSO, F., BIFERALE, L. & TOSCHI, F. 2017 Multiscale anisotropic fluctuations in sheared turbulence with multiple states. *Phys. Rev. Fluids* **2**, 052602(R).

JELLY, T.O., JUNG, S.Y. & ZAKI, T.A. 2014 Turbulence and skin friction modification in channel flow with streamwise-aligned superhydrophobic surface texture. *Phys. Fluids* **26**, 095102.

JIMÉNEZ, J. 2004 Turbulent flows over rough walls. *Annu. Rev. Fluid Mech.* **36**, 173–196.

JIMÉNEZ, J. & MOIN, P. 1991 The minimal flow unit in near-wall turbulence. *J. Fluid Mech.* **225**, 213–240.

KEVIN, K., MONTY, J. & HUTCHINS, N. 2019 The meandering behaviour of large-scale structures in turbulent boundary layers. *J. Fluid Mech.* **865**, R1.

KIM, K.C. & ADRIAN, R.J. 1999 Very large-scale motion in the outer layer. *Phys. Fluids* **11**, 417–422.

LEE, J., JELLY, T.O. & ZAKI, T.A. 2015 Effect of Reynolds number on turbulent drag reduction by superhydrophobic surface textures. *Flow Turbul. Combust.* **95**, 277–300.

LEONARDI, S. & CASTRO, I.P. 2010 Channel flow over large cube roughness: a direct numerical simulation study. *J. Fluid Mech.* **651**, 519–539.

LING, J., KURZAWSKI, A. & TEMPLETON, J. 2016 Reynolds averaged turbulence modelling using deep neural networks with embedded invariance. *J. Fluid Mech.* **807**, 155–166.

LOZANO-DURÁN, A. & JIMÉNEZ, J. 2014 Effect of the computational domain on direct simulations of turbulent channels up to $Re_\tau = 4200$. *Phys. Fluids* **26** (1), 011702.

MA, R., ALAMÉ, K. & MAHESH, K. 2021 Direct numerical simulation of turbulent channel flow over random rough surfaces. *J. Fluid Mech.* **908**, A40.

MACDONALD, M., OOI, A., GARCÍA-MAYORAL, R., HUTCHINS, N. & CHUNG, D. 2018 Direct numerical simulation of high aspect ratio spanwise-aligned bars. *J. Fluid Mech.* **843**, 126–155.

MARUSIC, I. & MONTY, J.P. 2019 Attached eddy model of wall turbulence. *Annu. Rev. Fluid Mech.* **51** (1), 49–74.

MAZZUOLI, M. & UHLMANN, M. 2017 Direct numerical simulation of open-channel flow over a fully rough wall at moderate relative submergence. *J. Fluid Mech.* **824**, 722–765.

MEDJNOUN, T., VANDERWEL, C. & GANAPATHISUBRAMANI, B. 2020 Effects of heterogeneous surface geometry on secondary flows in turbulent boundary layers. *J. Fluid Mech.* **886**, A31.

MEJIA-ALVAREZ, R. & CHRISTENSEN, K.T. 2013 Wall-parallel stereo particle-image velocimetry measurements in the roughness sublayer of turbulent flow overlying highly irregular roughness. *Phys. Fluids* **25** (11), 115109.

MENEVEAU, C. & MARUSIC, I. 2013 Generalized logarithmic law for high-order moments in turbulent boundary layers. *J. Fluid Mech.* **719**, R1.

MONTY, J.P., STEWART, J.A., WILLIAMS, R.C. & CHONG, M.S. 2007 Large-scale features in turbulent pipe and channel flows. *J. Fluid Mech.* **589**, 147–156.

NUGROHO, B., HUTCHINS, N. & MONTY, J. 2013 Large-scale spanwise periodicity in a turbulent boundary layer induced by highly ordered and directional surface roughness. *Intl J. Heat Fluid Flow* **41**, 90–102.

POPE, S.B. 2000 *Turbulent Flows*. Cambridge University Press.

RAUPACH, M., ANTONIA, R. & RAJAGOPALAN, S. 1991 Rough-wall turbulent boundary layers. *Appl. Mech. Rev.* **44** (1), 1–25.

SCHULTZ, M.P. & FLACK, K.A. 2007 The rough-wall turbulent boundary layer from the hydraulically smooth to the fully rough regime. *J. Fluid Mech.* **580**, 381–405.

DE SILVA, C.M., KRUG, D., LOHSE, D. & MARUSIC, I. 2017 Universality of the energy-containing structures in wall-bounded turbulence. *J. Fluid Mech.* **823**, 498–510.

SMITS, A.J., MCKEON, B.J. & MARUSIC, I. 2011 High-Reynolds number wall turbulence. *Annu. Rev. Fluid Mech.* **43** (1), 353–375.

VAN DER VEEN, R.C.A., HUISMAN, S.G., DUNG, O.Y., TANG, H.L., SUN, C. & LOHSE, D. 2016 Exploring the phase space of multiple states in highly turbulent Taylor–Couette flows. *Phys. Rev. Fluids* **1**, 024401.

VANDERWEL, C. & GANAPATHISUBRAMANI, B. 2015 Effects of spanwise spacing on large-scale secondary flows in rough-wall turbulent boundary layers. *J. Fluid Mech.* **774**, R2.

VIGGIANO, B., BOSSUYT, J., ALI, N., MEYERS, J. & CAL, R.B. 2022 Secondary motions above a staggered multi-scale rough wall. *J. Fluid Mech.* **941**, R1.

WANG, F. & LAM, K.M. 2019 Geometry effects on mean wake topology and large-scale coherent structures of wall-mounted prisms. *Phys. Fluids* **31**, 125109.

WILLINGHAM, D., ANDERSON, W., CHRITENSEN, K.T. & BARROS, J.M. 2014 Turbulent boundary layer flow over transverse aerodynamic roughness transitions: induced mixing and flow characterization. *Phys. Fluids* **26** (2), 025111.

WU, S., CHRISTENSEN, K. & PANTANO, C. 2019 Modelling smooth- and transitionally rough-wall turbulent channel flow by leveraging inner–outer interactions and principal component analysis. *J. Fluid Mech.* **863**, 407–453.

XIA, Z., SHI, Y., CAI, Q., WAN, M. & CHEN, S. 2018 Multiple states in turbulent plane Couette flow with spanwise rotation. *J. Fluid Mech.* **837**, 477–490.

XU, H.H.A., ALTLAND, S.J., YANG, X.I.A. & KUNZ, R.F. 2021 Flow over closely packed cubical roughness. *J. Fluid Mech.* **920**, A37.

YANG, J. & ANDERSON, W. 2018 Numerical study of turbulent channel flow over surfaces with variable spanwise heterogeneities: topographically-driven secondary flows affect outer-layer similarity of turbulent length scales. *Flow Turbul. Combust.* **100**, 1–17.

YANG, X.I.A. 2016 On the mean flow behaviour in the presence of regional-scale surface roughness heterogeneity. *Boundary-Layer Meteorol.* **5**, 1–17.

YANG, X.I.A. & MENEVEAU, C. 2016 Large eddy simulations and parameterisation of roughness element orientation and flow direction effects in rough wall boundary layers. *J. Turbul.* **17** (11), 1072–1085.

YANG, X.I.A. & MENEVEAU, C. 2017 Modelling turbulent boundary layer flow over fractal-like multiscale terrain using large-eddy simulations and analytical tools. *Proc. R. Soc.* A **375** (2091), 20160098.

YANG, X.I.A., SADIQUE, J., MITTAL, R. & MENEVEAU, C. 2016 Exponential roughness layer and analytical model for turbulent boundary layer flow over rectangular-prism roughness elements. *J. Fluid Mech.* **789**, 127–165.

YANG, X.I.A., XU, H.H.A., HUANG, X.L.D. & GE, M.-W. 2019 Drag forces on sparsely packed cube arrays. *J. Fluid Mech.* **880**, 992–1019.

YUAN, J. & PIOMELLI, U. 2014 Roughness effects on the Reynolds stress budgets in near-wall turbulence. *J. Fluid Mech.* **760**, R1.

ZHANG, W., ZHU, X., YANG, X.I.A. & WAN, M. 2022 Evidence for Raupach *et al.*'s mixing-layer analogy in deep homogeneous urban-canopy flows. *J. Fluid Mech.* **944**, A46.